Atherectomy-Soft Tissue Machining

December 16th, 2014

Prepared by Team 6

Di Fu

Fangzhou Xia

Huijiao Guan

Sing Kiet Kong

Xingjian Lai

Undergraduate Engineers, University of Michigan College of Engineering

Prepared For

Dr. Roland Chen

ME 482 Instructor Department of Mechanical Engineering

University of Michigan College of Engineering

Executive Summary

Atherectomy is a minimally invasive surgery to remove plaque off the artery wall to treat cardiovascular disease (CVD). This method is mainly focused on treating peripheral arterial disease (PAD), which refers to atherosclerosis affecting the peripheral arterial system [1]. Atherosclerosis is the accumulation of fatty and calcified plaque on the artery wall, which when left unattended, results in the narrowing and hardening of the artery.

Although atherectomy has its advantage of being minimally invasive, the method suffers a high complication rate. This project aims to investigate the plague grinding mechanism for future device development and surgical planning. Emphasis will be laid on Rotational Atherectomy (RA) technique with the Diamondback 360® Orbital PAD System (DB360). This method ablates plaque with a rotating diamond-coated crown which is mounted eccentrically on a single use catheter [2]. Complications might arise from the motion of the rotational crown, in which the magnitude of the grinding vibration force changes with increasing lumen diameter. To investigate these problems, this project focuses on three aspects, namely the artery fabrication, grinding vibration force measurement, and the orbiting frequency.

For the artery fabrication, arterial wall made of PVC was successfully fabricated. To model the actual condition during micro-grinding process inside human artery, PDMS was tested as a potential arterial wall phantom material. However, it was hard to peel a thin layer of PDMS off the aluminum rod without rolling on itself. A proposed solution was to coat the aluminum shaft with PVC before putting it into PDMS so that a thin layer of PVC allows easier aluminum shaft removal and thereby forming the artery.

Data collection of the dynamometer was improved by introducing a LabVIEW data acquisition system at a sampling rate of 5,000 Hz. This LabVIEW system provides a convenient way of comparing and verifying the data acquired throughout the experiment. Using MATLAB to conduct an analysis on the video captured using a high speed camera, the motion of the grinding wheel and the driving shaft were tracked and observed. The deformation of the arterial phantom wall was also analyzed. The Fast Fourier Transform was then conducted for frequency analysis.

The driving shaft vibration was also investigated by the team. Both static and dynamic analyses were conducted. For the static analysis, the beam theory was applied. The static analysis model equations are in general easy to solve for estimation of the tip deflection for the first half wavelength of the driving shaft but does not reflect the actual wave and vibration situation. For the dynamic analysis, the dynamic term of the beam was considered. An equation was obtained in the end but the 4th order partial differential equation involved does not have an easy solution and is beyond the scope of this project. An alternative method of predicting the shaft vibration model is to analyze the geometry of shaft vibration from video captured during experiments and substitute the vibration geometry in the dynamic beam theory.

The rigidity of the driving shaft plays an important role in the theoretical model of the driving shaft vibration. Therefore, a “Four-Point Bending Test” was conducted to measure the rigidity. A high resolution camera and MATLAB Image Tool were used to collect and analyze the data. The rigidity of the shaft was determined to be about 4045 N-mm^2.

Despite the great result, future work still needs to be done to refine the result of each experiment.

Table of Contents

1 Introduction

Peripheral arterial disease (PAD) refers to atherosclerosis which affects the peripheral arterial system [3]. Atherosclerosis is the accumulation of fatty and calcified plaque on the artery wall, which is common in patients with diabetes, renal insufficiency, and a history of smoking [1]. The development of atherosclerosis results in the narrowing and hardening of the artery.

To treat obstructive atherosclerotic disease, Rotational Atherectomy (RA) technique with the Diamondback 360® Orbital PAD System (DB360) is introduced. RA ablates plaque with a diamond-coated crown rotating at high speed (up to 200,000 rpm), which is mounted eccentrically on a single use catheter [1]. The abrasive crown is able to ablate inelastic plaque without hurting the elastic artery wall due to the principle of differential sanding. As the rotational crown advances gradually across a lesion over a guide wire, compliant tissues stretch away from the crown, while rigid calcified plaque provides resistance allowing for sanding [1]. As a result, RA yields a smooth luminal surface with cylindrical geometry and minimal tissue injury [4].

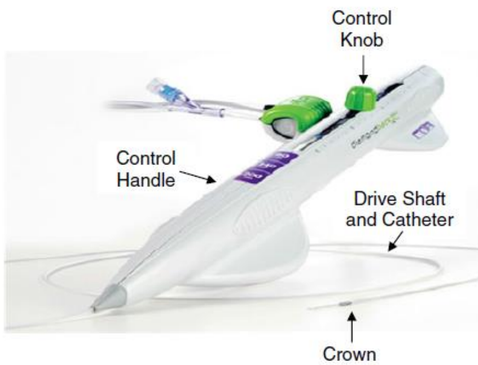

Figure 1: Components of the Diamondback 360 ºPAD System

Despite RA's superiority in treating heavily calcified plaque, which varies significantly between different patients in hardness depending on the degree of calcification, high clinical complication rates in RA have been reported. Such complications include vascular access complications, angiographic complications, vasospasm, and burr entrapment [4].

To investigate the high clinical complication rates, the motion of the rotational crown was analyzed. The crown centrifugal force was simulated using finite element method [1]. The analysis demonstrated that as the plaque was being removed, the centrifugal force first increased, reached a peak, and then decreased with increasing lumen diameter [1].

This project will focus on three aspects, namely the artery fabrication, centrifugal cutting force measurement, and the orbiting frequency. Besides PVC, other transparent materials with Young's modulus similar to the artery wall will be selected to better mimic human artery. As for the crown motion during the grinding process, hands-on experiments will be conducted and the results will be compared against established models in previous studies.

2 Experiment Methods

2.1 Experiment Setup

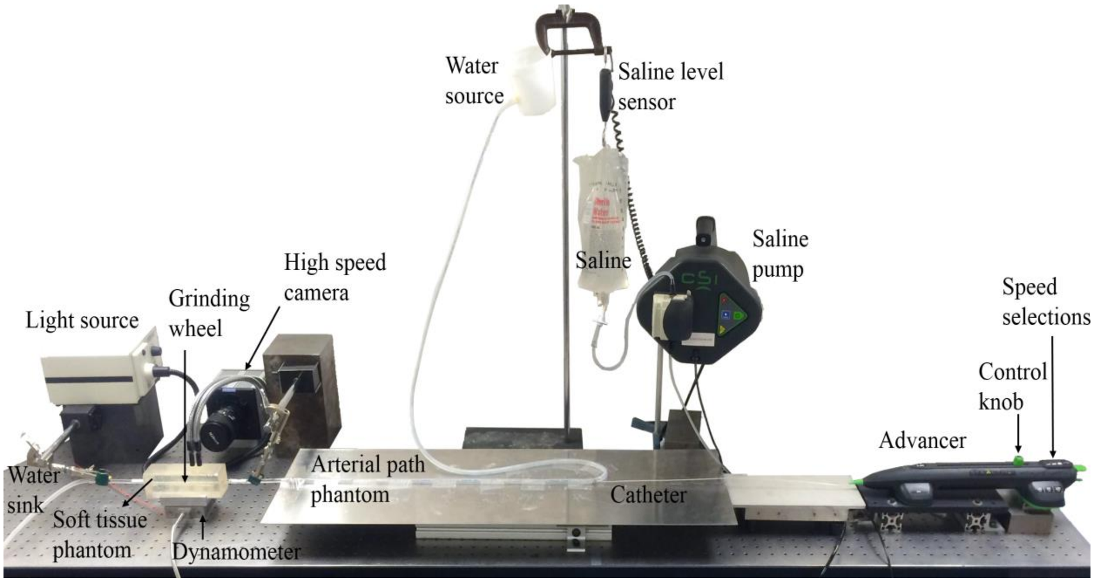

Figure 2: Experiment Setup

The original experimental table setup is shown in Figure 2. In general, the grinding system driver is located on the right hand side of the picture. The arterial path phantom and fluid source are located in the middle. The left hand side of the picture involves the measurement devices and corresponding supplementary device. The Diamondback 360 ºPAD System as shown in Figure 1 is used for driving the grinding wheel of the test system.

The system involves two types of fluid, namely water and saline as shown in the middle of Figure 2. The saline is used for the grinding system cooling while water is used to mimic the blood within the artery.

The measurement device of the system involves a Kistler 9256 C dynamometer rigidly connected to the arterial and soft tissue phantom to record the force induced by the motion of the grinding wheel. A high speed camera with light source is also included to capture the motion of the grinding wheel in real time.

Data collection of the dynamometer was conducted by LabVIEW data acquisition system at a sampling rate of 5,000 Hz. The high speed camera is recording the video at the speed of 10,000 frame per second using the corresponding software provided by the vendor. The data collection systems are synchronized by using LabVIEW to capture the mouse click activity within a certain range on the screen to start the high speed camera video recording. The synchronization of data collection is important in this case as it provides a convenient way of comparing and verifying the data. Moreover, the radial force and tangential force can be decoupled by capturing the instance when the grinding wheel is at the top or bottom of the circular artery phantom for radial load and when the grinding wheel is at the left or right most end of the artery phantom for tangential load.

2.2 Experiment Table Improvement

There are two complication involved in the original setup. The first complication lies in the measurement data of dynamometer as it involved significant noisy which made it impossible to isolate the force caused by the motion of the grinding bit. The supposed reason to this phenomenon was assumed to be the vibration of the Diamondback 360 ºPAD System passed through the workbench such that dampers and mass needed to be added to the dynamometer fixture and a mechanical structure was designed to resolve the problem. Before implementing the design in the machine shop, the major reason for the noise in the signal was identified to be the insulation of the dynamometer base with the ground and was resolved electronically by a conducting cable.

The second complication lies in the adjustment of the height of the arterial path phantom as the original setup involves stacking several pieces of aluminum plate to reach a specific height, which is both material consuming and hard to adjust due to the discrete thickness of the plates. A new design using T-slotted aluminum framing was proposed and has been implemented as shown in Figure 4. This design allowed free adjustment of height of the arterial path phantom to compensate for different sizes of the soft tissue phantom mounted on the fixed dynamometer fixture.

During the semester, the test setup fixtures have been redesigned as shown in Figure 3 and Figure 4. The height adjustable setup allows the easy change of the artery size to give different boundary conditions.

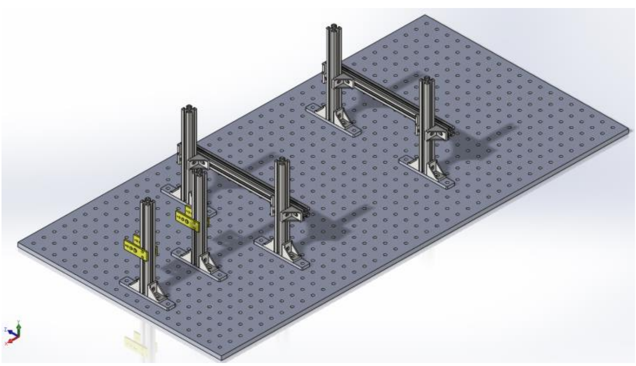

Figure 3: Height Adjustable Artery Fixture CAD

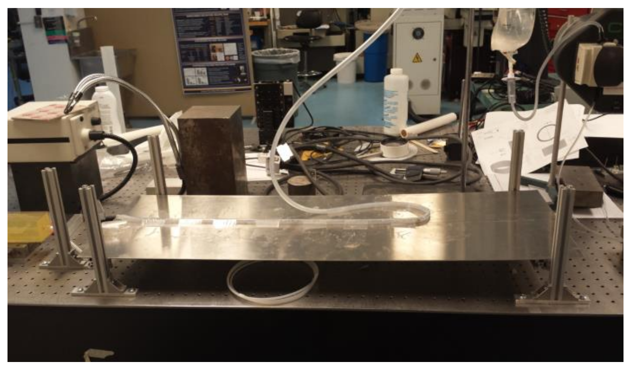

Figure 4: Fixture Structure Assembly

2.3 Arterial Phantom

The current soft tissue phantom, as shown in Figure 5(a), consists of arterial wall phantom, muscle phantom, and a polycarbonate (PC) shell, with dimensions shown in Figure 5(b). The arterial wall is made of Polyvinyl chloride (PVC) (Young's modulus: 45kPa) while the muscle phantom is made of PVC and softener mixture (Young's modulus: 8kPa).

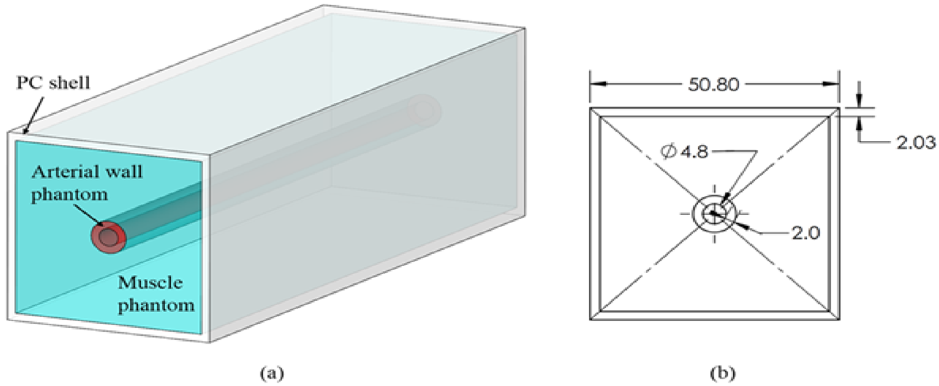

Figure 5: Soft Tissue Phantom: (a) Sections (b) Dimensions

To fabricate the current soft tissue phantom, the PVC plastisol was heated to 150 ℃ until the white plastisol turned transparent (about 20mins). Then the liquid was degased in a vacuum chamber at -90 kPa for 10 minutes. An aluminum rod was dipped into the PVC liquid and a thin layer of the PVC liquid would stick and cure on the rod, resulting in the formation of the arterial wall phantom (Figure 6). This arterial wall phantom together with the aluminum rod inside was put in the middle of the PC shell. The PVC plastisol mixed with a softener in a ratio of 1:1 was heated at 150 ℃ for 20 minutes and then degased in vacuum chamber at -90 kPa for 20 minutes. The mixture was poured into the PC tube to form the muscle phantom. The aluminum rod was removed after the PVC liquid was cooled to the room temperature.

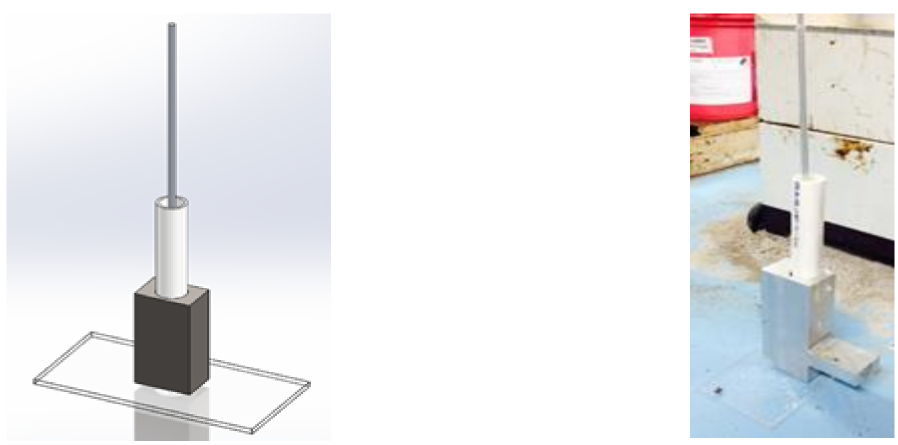

Figure 6: (a) Dipping aluminum rod into PVC liquid (b) Experiment Setup

2.3.1 Arterial Phantom Improvement with Polydimethylsiloxane (PDMS)

In order to model the actual condition during micro-grinding process inside human artery, a crucial part is to pick the right material to construct an artificial tubing that highly resembles artery properties. Factors that need to be considered includes safety, cost, density, stiffness, physical strength, and etc. Current study in our lab utilizes tissue-mimicking soft polyvinyl chloride (PVC) to simulate as artery. Even though many experiments have been carried out using the PVC, it is still not an ideal approximation for soft tissue since the tensile Young's Modulus of the arterial wall phantom (45kPa) is much lower than that of the real tissue (~2000kPa). To solve the problem, polydimethylsiloxane is tested for the arterial wall phantom. The young's modulus of PDMS is much higher than PVC and it is flexible (1320 – 2970kPa) depending on the mixture ratio, curing temperature and time.

To fabricate the arterial wall phantom using PDMS, The PDMS liquid was first mixed with a hardener in ratios of 5:1, 10:1, 20:1, and 30:1. The 4 cups of mixture were then degased in vacuum chamber at -90 kPa for 10 minutes to remove bubbles. After that, 4 aluminum rods were dipped into the 4 mixtures, heated at 80 ℃, and then cooled to room temperature to form the arterial wall. With increasing ratio of PDMS liquid, the arterial wall became softer. However, it was hard to peel a thin layer of PDMS off the aluminum rod without rolling on itself.

A mimic of the muscle phantom outside the arterial wall phantom by surrounding the hardening PDMS with PVC liquid was created. When the PVC cured, the PDMS arterial wall phantom was observed not to stick to the outer PVC muscle phantom.

One problem left to be resolved with PDMS so that it can actually be used for the phantom is the sticky issue of PDMS on the aluminum shaft which makes the removal of the aluminum shaft very difficult. A proposed solution is to coat the aluminum shaft with PVC in advance before putting it into PDMS so that a thin layer of PVC allows easier removal of the aluminum shaft and thereby forming the artery.

2.4 Driving Shaft Rigidity Measurement Setup

From the experiment conducted, the value of the driving shaft bending stiffness, which is an important parameter of the driving shaft, was needed for modeling purpose. Because of the complex geometry of the shaft involving coils of spring going around the driving shaft, the traditional equation to calculate the area moment of inertia does not give an accurate result due to the separation between the driving shaft and the coils. Therefore, the rigidity (EI) of the shaft needs to be determined experimentally.

The fundamental idea of the test is using a "Four-Point Bending Test". As shown in Figure 7(a) the shaft is supported by two thin metal sheets. Two equal loads are applied at the two ends of the shaft. Due to the force, the shaft will be bent and there will be a displacement in the y axis (Figure 7(b)). Also, the force will generate a bending moment on the shaft. The shaft stiffness will be calculated by varying the bending moment and measuring the coresponding displacement. The bending moment is varied by changing the force at the ends; its numercial value is the product of the bending force and the moment arm.

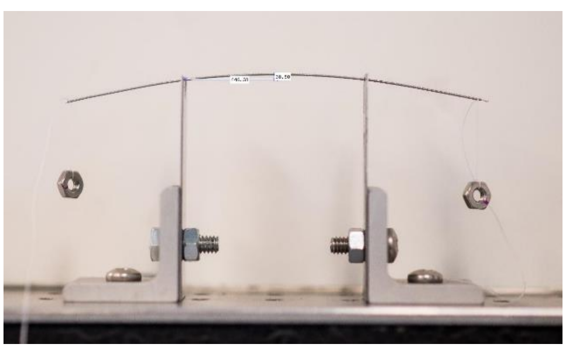

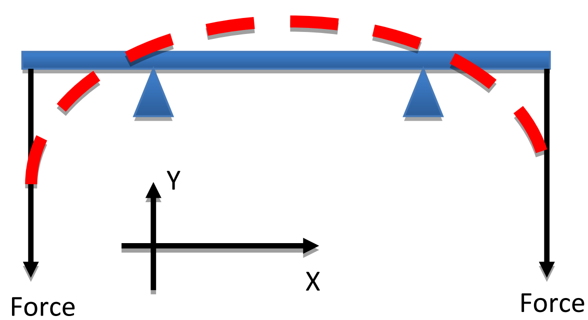

Figure 7: (a) The four point bending test setup. (b) The schematic of the four-point bending test

In order to measure the moment arm distance and the bending deflection, a high resolution camera and MATLAB Image Tool are used. The image tool can provide the number of pixels between two points. In order to measure the distance through the pixel number, a calibrition is required (Figure 8). The number of pixels between a distance of 10 mm is found with the image tool. Thus, the moment arm and the deflection can be identified by the number of pixels between the two points.

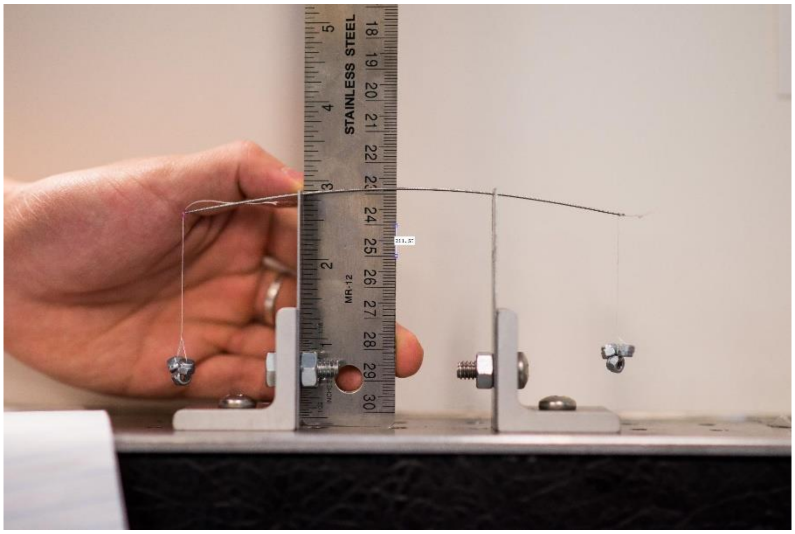

Figure 8: The calibration process of the four-point bending test

2.5 Experimental Design and Procedure

2.5.1 Testing Procedure

During the grinding test, a constant flow of saline solution lubricated the device and flushed the artery. The grinding wheel was capable of rotating in three levels of speed: low (60,000 rpm), moderate (90,000 rpm), and high (120,000 rpm). At each rotational speed, a high speed camera recorded the movement of the grinding wheel and the deformation of the arterial soft phantom at a frame rate of 10,000 fps. The dynamometer was placed under the arterial phantom to measure the grinding force in the vertical direction.

Data collection of the dynamometer was conducted by LabVIEW data acquisition system at a sampling rate of 5,000 Hz. The high speed camera recorded the video at the speed of 10,000 frame per second using the corresponding software provided by the vendor. The data collection systems are synchronized by using LabVIEW to capture the mouse click activity within a certain range on the screen to start the high speed camera video recording. The synchronization of data collection is important in this case as it provides a convenient way of comparing and verifying the data. Moreover, the radial force and tangential force can be decoupled by capturing the instance when the grinding wheel is at the top or bottom of the circular artery phantom for radial load and when the grinding wheel is at the left or right most end of the artery phantom for tangential load.

After the grinding test, the video was processed in MATLAB. The grinding wheel motion was tracked through the movement of two points: the midpoint of one edge of the grinding wheel as well as the connection point between the grinding wheel and shaft. Through these two points the motions of both grinding wheel and driving guide wire were observed. Also, the deformation of the arterial phantom wall was analyzed through the video processing. After the video image processing, the Fast Fourier transform was conducted for frequency analysis.

3 Experiment Result

3.1 Grinding Wheel Motion

The position of connection point for 23.3 ms (419 frames) at 90, 000 rpm grinding wheel rotational speed can be seen in Figure 9(a). The graph demonstrates a combination of motion of a high and low frequency. The motion of the connection point from 11.1 to 11.8 ms is shown in Figure 9(b). The image at 9 time instances with 0.08 ms time step is shown in Figure 9(c). These figures show the connection point circled around an axis in the grinding wheel.

By using FFT of the motion data in Figure 9(a), Figure 10(a) can be generated. At 90,000 rpm rotational speed of the grinding wheel, we can observe a high frequency motion was 1,500 rpm, and a low frequency at 41.2 Hz. The low frequency indicates the grinding wheel orbited around the vessel phantom.

By applying the same 23.3 ms time period and the motion of the grinding wheel is shown in Figure 9(d). The corresponding 9 images with 2.9 ms time step is shown in Figure 9(e) and clearly demonstrated that the grinding wheel orbited inside the vessel lumen. The grinding wheel did not exhibit the 1,500 Hz high frequency motion. FFT analysis of the grinding wheel motion in this case (Figure 10(b)) showed 41.8 Hz orbiting frequency, close to the 41.2 Hz of the connection point.

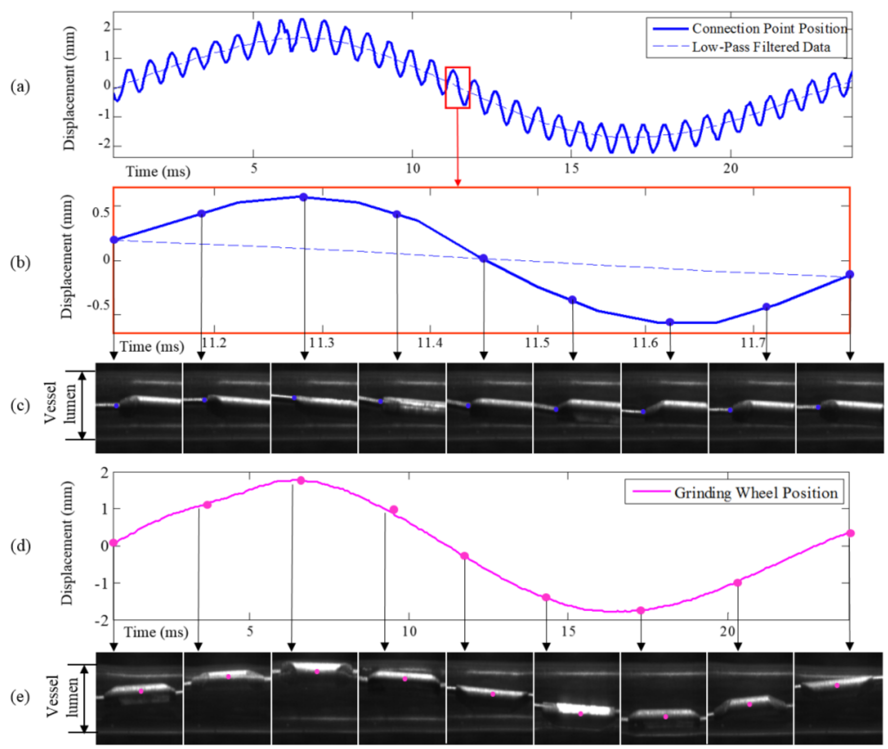

Figure 9: The connection point (a) motion, (b) zoom-in view of a high-frequency period, and (c) corresponding images and the grinding wheel point (d) motion and (e) corresponding images.

Table 1 summarizes the mean and standard deviation (SD) of the high and low frequencies motion of the connection point in the five tests at three rotational speeds (60,000, 90,000, and 120,000 rpm). The orbital frequency increased from 19.3 to 38.3 Hz from 60,000 to 90,000 rpm. When the grinding wheel speed increased to 120,000 rpm, the increase in orbiting frequency was small, only to 40.5 Hz. The rotation frequency of the connection point is related with the rotational speed at 60,000 rpm. Possibly because of the instability of the electrical motor or the lubrication inside the catheter, the high rotation frequency varied between 1660 and 1870 Hz at 120,000 rpm. The SD was small (less than 5% of the mean value) for the five tests and demonstrated the consistency of the experiment.

Figure 11 contains images of the 90,000 rpm grinding wheel with the high-speed camera imaging from the front (along the vessel axis). Figure 11(a) studies the grinding wheel point, which orbited around the vessel in the same direction as its rotational direction with a period of 24ms. This finding matches with the rotational direction observed from the side (Figure 9). Figure 11(b) traces the connection point and sees that, in about 0.72 ms, the grinding wheel rotated around its centerline axis. The shaft connection point gyrated in a radius that equaled to the distance between the drive shaft and grinding wheel axis, and induces the vibration of the drive shaft.

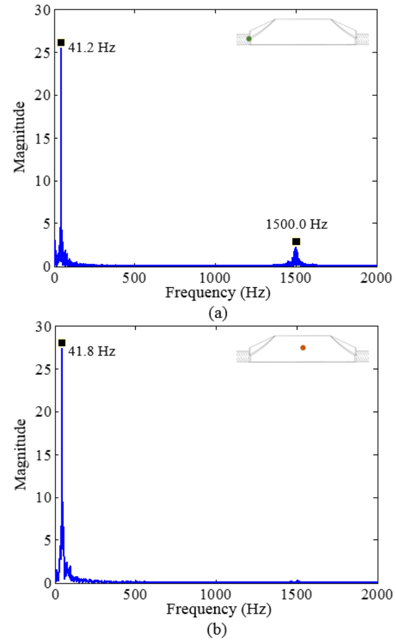

Figure 10: Grinding wheel motion frequency analysis: (a) the connection point and (b) the grinding wheel point

Rotational Speed /rpm	Frequency	Mean (Hz)	SD (Hz)
60,000	Orbiting (low)	19.3	0.6
	Rotation (high)	1003.4	8.5
90,000	Orbiting	38.2	1.7
	Rotation	1499.6	3.0
120,000	Orbiting	40.5	0.4
	Rotation	1660-1870	-

Table 1: Grinding wheel orbiting (low) and rotation (high) frequencies at three rotational speeds

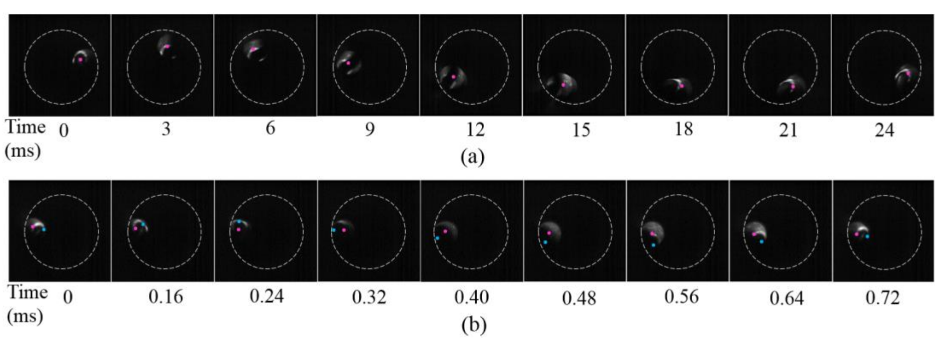

Figure 11: Front view of grinding wheel motion at 90,000 rpm: (a) one orbital cycle and (b) one rotational cycle. (grinding wheel point in magenta color, connection point in turquoise color, and vessel lumen in circle)

3.2 Shaft Rigidity Measurement Result

As the stiffness of the shaft is an important variable in the mathematical and the shaft is not a regular shaped rod, an experiment to determine the stiffness of the shaft has been conducted.

Six different loads are applied on the two ends of the shaft. Using the MATLAB Image tool, the corresponding moment arm distance (L), support distance (S) and deflection (y) are measured (Table 2).

Load (g)	Force (N)	Moment Arm (mm)	Moment (N-mm)	Deflection (mm)
0.322	0.003	69.527	0.2196	0.473
0.795	0.008	70.473	0.5496	1.087
1.240	0.012	70.236	0.8544	1.584
1.366	0.013	69.433	0.9304	1.820
1.936	0.019	67.683	1.2854	2.435
4.583	0.045	64.894	2.9176	5.118

Table 2: The corresponding moment and deflection for different load

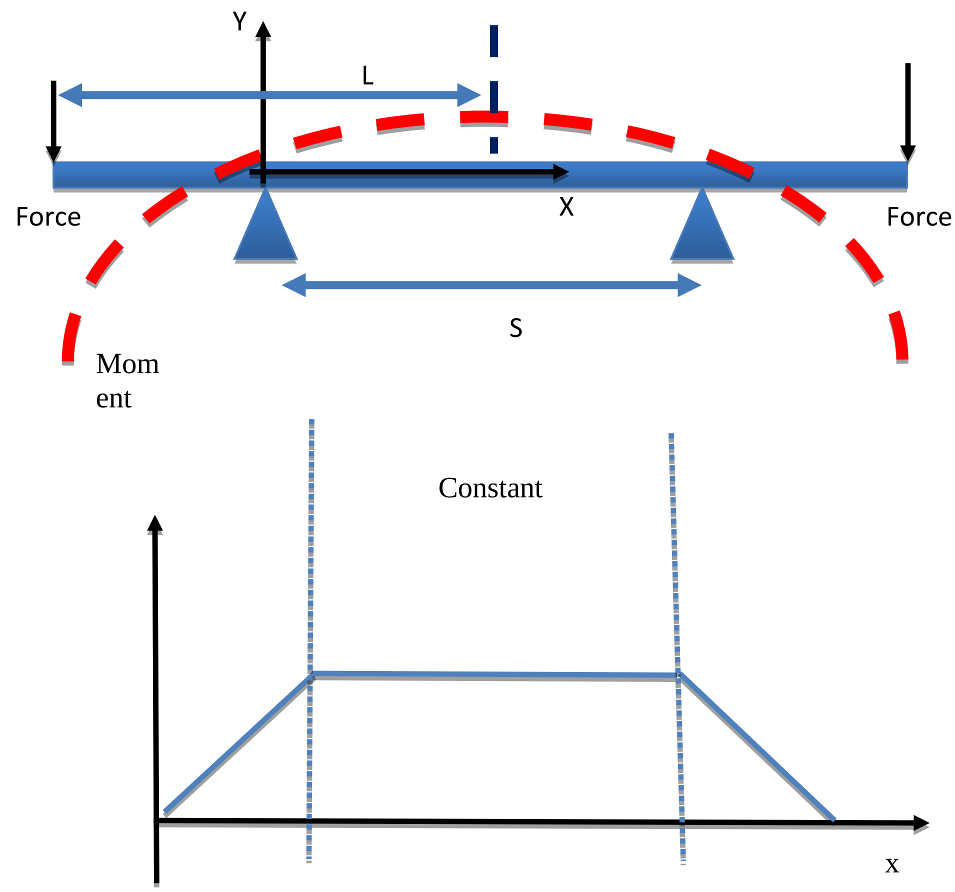

Figure 12: The bending diagram of the four-point bending test. S = 61.12mm

The governing equation to calculate the rigidity (EI) of the shaft is shown below.

$$\frac{d^2y}{dx^2} = \frac{M(x)}{EI} \qquad \text{Equation 1}$$

However, when 0 < x < S, the bending moment of the shaft is constant. The bending diagram is shown Figure 12. Due to the simple support, there is no deflection when x = 0 or x = S. After applying the boundary condition, the differential equation can be solved.

$$y = \frac{M}{EI}x^2 - \frac{MS}{EI} \qquad \text{Equation 2}$$

Since the deflection is measured at the mid point between the two supports, x should be $\frac{S}{2}$. Therefore,

$$M = -\frac{2EI}{S^2}y \qquad \text{Equation 3}$$

Moment vs defelction curve is plotted in Figure 13. According to Equation 3, the slope of the curve is $\frac{2EI}{S^2}$. The negative sign is elimated because the moment is negative. From the plot, the slope is 1.7139. Therefore, the rigidty of the shaft is about 4045 N-mm^2.

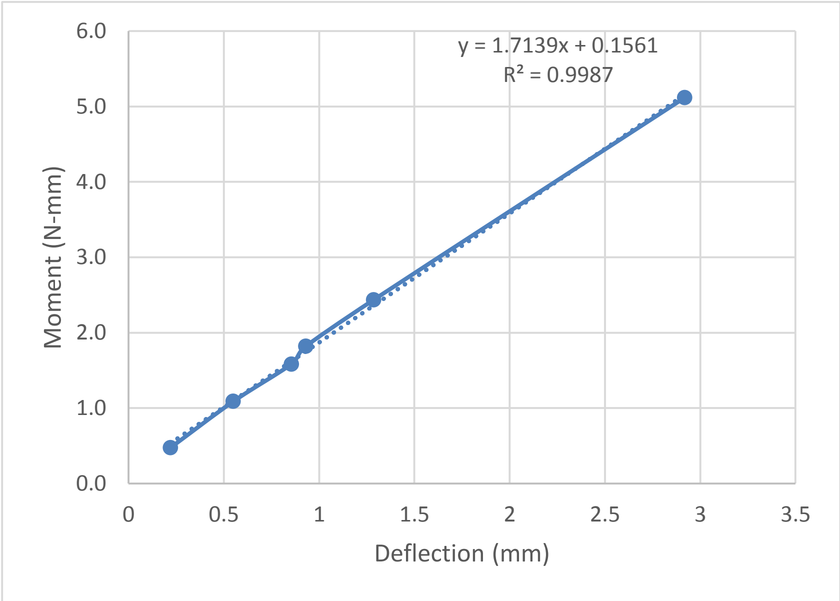

Figure 13: Moment vs Deflection curve

4 Discussion

4.1 Motivation of Shaft Vibration Model

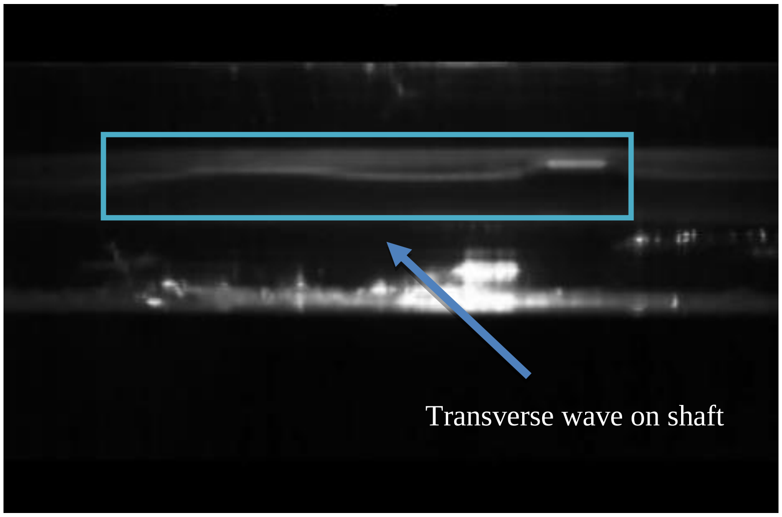

Figure 14: Transverse Wave Observed on Shaft

As shown in Figure 14, the driving shaft is observed to have a transverse wave going along the shaft. The current testing results indicate that there is a high-frequency vibration and a low-frequency orbital motion. The team is interested in investigating the high frequency vibration as the normal force of the grinding bit leaning against the wall is closely related to the net force on the grinding wheel due to vibration and the reaction force exerted by the driving shaft during high frequency vibration. The underlining assumption is that the high frequency is caused by the orbital motion of the grinding bit. The grinding wheel was driven by the shaft transmitting torque from the electric motor. The connection point between the shaft and the wheel will gyrate in a radius of distance to the rotational axis, which eventually will cause the vibration of the shaft. More tests will be conducted by varying the rotational speed, inner diameter of the artery and the length of the guide wire to see how these variables will affect the vibration frequency.

Literature review was conducted to search for a mathematical model that can explain predict the vibration and transverse wave on the driving shaft. This phenomenon can be visualized as a person waving one end of the rope really fast. You can imagine that the maximum amplitude of the rope wave is much bigger than the initial displacement on one end.

4.2 Shaft Vibration Model

To model the shaft vibration, several different approaches have been taken. In all modeling scenario, the fluid dynamics effect and gravity terms were not included to avoid solving complicated partial differential equation. The first approach is by static analysis of the shaft with beam theory. This model has the advantage of being easy to solve in terms of the ordinary differential equation but does not reflect the motion observed from the experiment. The second model considers the dynamic effect of beam theory by involving the acceleration terms. To simplify the problem, the wave differential equation is modeled in

2D. This model theoretically includes the general effect of the system but has the drawback of being complicated in solution.

4.2.1 Static Analysis

The first approach taken by the team to model the driving shaft behavior is to apply the beam theory to the shaft with the assumption that the deformation of the beam is uniform in steady state. The problem setup is shown in Figure 15. The assumptions utilized for this model are listed as:

1. Deflection of driving shaft is small
2. Beam theory is still valid
3. Gravity is negligible
4. Steady state exists

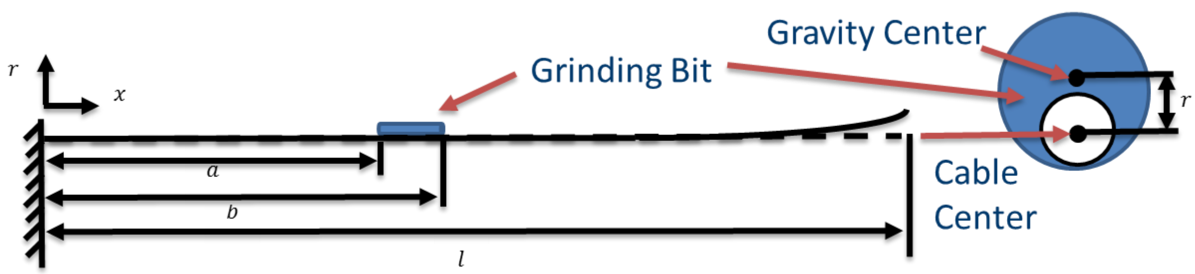

Figure 15: Shaft Analysis Model

Based on the assumptions and classical beam theory, the equations for calculating the deflection of the driving shaft were obtained in Equation 4 and can be solved with proper implementation of boundary conditions by direct integration.

$$\begin{cases} EI\dfrac{d^4r}{dx^4} = \omega^2\rho A\cdot r, & 0 \le x \le a \\ EI\dfrac{d^4r}{dx^4} = \omega^2\rho A\cdot r + \omega^2\rho_g A_g(r+d), & a \le x \le b \\ EI\dfrac{d^4r}{dx^4} = \omega^2\rho A\cdot r, & b \le x \le l \end{cases} \qquad \text{Equation 4}$$

A more simplified model was also obtained based on Equation 4 by taking the grinding wheel as a mass point and the driving shaft bending rigidity simplified to a constant K. The assumptions in addition to the original static analysis is given as:

1. Forces due to cable inertia and gravity are neglected.
2. Mass of the grinding bit is concentrated at a point.
3. Flexural rigidity is determined experimentally as K for different level of deflection and geometry and extrapolated.

The simplified equation was shown in Equation 5.

$$m\omega^2(r+d) = Kr \quad \text{Equation 5}$$

The static analysis model equations are in general easy to solve for estimation of the tip deflection for the first half wavelength of the driving shaft but does not reflect the actual wave and vibration situation.

4.2.2 Dynamic Analysis

To model the observed motion of the driving shaft in a more accurate manner, the dynamic term of the beam is considered. All model assumptions remained the same except for the steady state assumption in the static analysis case for the model to yield Equation 6 [6].

$$EI\frac{\partial^4 y}{\partial x^4} + \rho A \cdot \frac{\partial^2 y}{\partial t^2} = w,\ \ with\ w = 0 \quad \text{Equation 6}$$

The 4th order partial differential equation involved in the model does not have an easy solution and might be solved analytically using Fourier Transformation with respect to time and solving a fourth order ordinary differential equation. The analytical solution of the equation is beyond the scope of the project and a parameter estimation method for wave characteristic was proposed and discussed in the next section.

4.2.3 Prediction from Measurement Result

An alternative method of predicting the shaft vibration model is to analyze the geometry of shaft vibration from video captured during experiments and substitute the vibration geometry in the dynamic beam theory (Equation 6). The video shows that the gyration of the connecting point between the shaft and the grinding wheel generates a sinusoidal transverse wave on the shaft. Neglecting the fluid resistance, the wave is assumed traveling indefinitely, with no loss of energy.

The general function of sinusoidal wave *(y)* with respect to time *(t)* and spatial coordinate *(x)* is shown in Equation 7 [7].

$$y(x,t) = Acos(\frac{2\pi t}{T} - \frac{2\pi x}{\lambda}) \quad \text{Equation 7}$$

where A is amplitude of wave, T is time period, and λ is spatial wavelength.

The time period of the wave is estimated by observing the wave propagation at different frames. Figure 16 shows the wave shape at frame 910, 950, 990, and 1050. Even though the shaft and grinding wheel keep moving up and down due to the orbital motion of the grinding wheel, the wave shape stays unchanged every 10 frames. The time period can be then calculated using Equation 8.

$$T = \frac{10\ frames}{10k\ frames/second} \quad \text{Equation 8}$$

The amplitude and wavelength can be estimated by observing frames with peak and valley and measure the distance using pixel, which is shown in Figure 17. The length can be calculated using Equation 9. For Figure 17, the dpi is 96 (38 dpcm).

$$length = \frac{pixel}{dpi\ (dots\ per\ inch)} \quad \text{Equation 9}$$

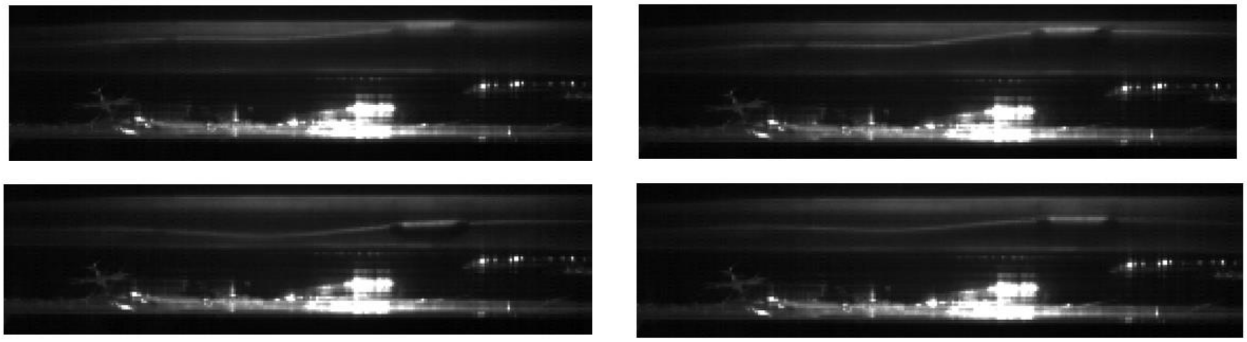

Figure 16: Wave Propagation at frame 910 (upper left), 950 (upper right), 990 (lower left), and 1050 (lower right)

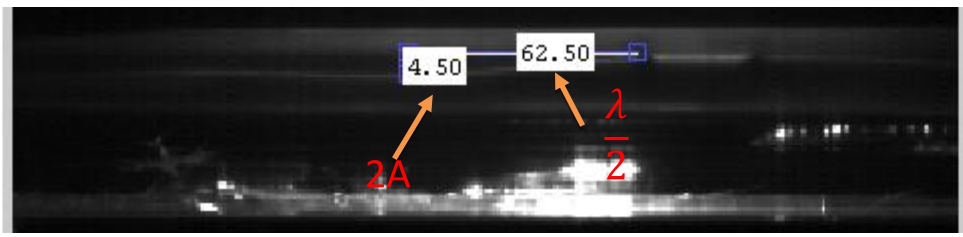

Figure 17: Measurement of wave amplitude & wavelength using pixel

With all the parameters specified, the movement of the sinusoidal wave is predicted in Equation 10.

$$y(x,t) = 6.25 \times 10^{-4} cos(2000\pi t - 60.81\pi x) \qquad \text{Equation 10}$$

By substituting the wave function (Equation 10) in the dynamic Euler-Bernoulli beam theory (Equation 6), the following equivalence should be arrived at any position and time (Equation 11).

$$(EI\beta^4 - \rho A_s \omega^2)\text{A}\cos(\omega t - \beta x) = w, \;\; with\, w = 0 \qquad \text{Equation 11}$$

Where EI is the measured shaft stiffness, $\beta = \frac{2\pi}{\lambda}$ is phase constant, $\omega = \frac{2\pi}{T}$ is angular frequency, ρ is shaft density, and A_s is sectional area of shaft.

Stiffness [N-m^2]	EI	4.045E-03
Amplitude [m]	A	6.250E-04
phase constant [rad/m]	β	1.910E+02
Angular Frequency [rad/s]	ω	6.283E+03
Shaft Density [kg/m^3]	ρ	8.030E+03
Shaft Area [m^2]	A_s	4.902E-07

Table 3: Parameters for Calculation

However, with parameters specified in Table 3, the coefficient of the cosine function in left hand side is calculated to be 3270, which is much higher than 0. The error may come from the following factors:

1. The inaccuracy of the predicted wave function. This may come from the errors of both the video itself and the video analysis. Also, the energy is assumed conservative during wave propagation. However, the fluid resistance will dissipate the wave energy and result in a lossy sinusoidal wave. The general function of a sinusoidal wave in lossy medium is shown in Equation 12 [7], which is different from what has been used.

$$y(x,t) = Ae^{-\alpha x} cos(\frac{2\pi t}{T} - \frac{2\pi x}{\lambda}) \qquad \text{Equation 12}$$

where α [Np/m] is the attenuation factor.

2. The property of the driving shaft. As shown in Figure 18, the driving shaft is made of six coils helically wound the guidewire with a 0.79mm OD. The geometry of the sectional area is simplified as a circle with diameter of 0.79mm in the model. However, it is more complicated as shown in the figure. Also, the density used in the model is for stainless steel, which is the material for guidewire. The outer coils are not considered.

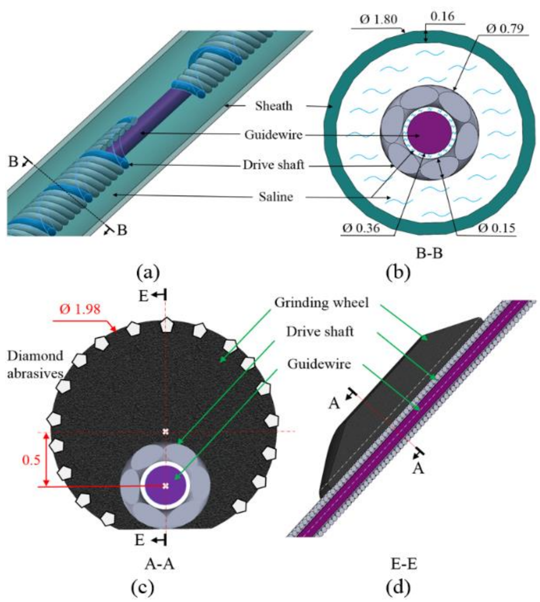

Figure 18: Geometry of the Drive Shaft

3. The inaccuracy of the dynamic beam theory. To use the beam theory, the shaft vibration is simplified from 3D to 2D with some assumptions. Also, the influence of the fluid is not considered.

5 Future Work

The Atherectomy-Soft Tissue Machining process study has covered three major aspects: artery fabrication, centrifugal cutting force measurement, and orbit frequency analysis. Despite the great results, future work still remains to improve better analyze the grinding process. The timeline and job allocation can be found in section 3.5 of the report.

5.1 Artery Fabrication Using PDMS

As mentioned above (Section 2.3.1), the tensile Young's Modulus of current artery-mimicking material PVC (45kPa) is much lower than that of the real tissue (~2000kPa). To improve the artery performance, PDMS is considered for its higher and flexible (1320-2970kPa) Young's Modulus. However, during experiments, PDMS is observed sticky to the aluminum shaft, which makes the removal of the aluminum shaft very difficult. A proposed future plan is to coat the aluminum shaft with PVC in advance before putting it into PDMS so that a thin layer of PVC allows easier removal of the aluminum shaft and thereby forming the artery.

5.2 Shaft Vibration Modeling

The current method of predicting the shaft vibration model is to analyze the geometry of shaft vibration from video captured during experiments and substitute the vibration geometry in the dynamic beam theory (Equation 6). However, with the wave propagation on the shaft specified, the shaft vibration does not satisfy the dynamic beam theory with nonzero coefficient on the left hand side. Errors coming from three possible factors are analyzed. For future work, more experiments and literature reviews should be conducted to decide which the leading factor is.

5.2.1 Accuracy Improvement of the Predicted Wave Function

To improve the wave function modeling, videos with higher resolution should be captured and more frames should be used to reduce the errors in wave amplitude and wavelength analysis. Also, the general function of a sinusoidal wave in lossy medium (Equation 12) can be applied to take the energy loss during wave propagation into consideration.

5.2.2 Property of the Driving Shaft

In current model, the geometry of the sectional area is simplified as a circle with diameter of 0.79mm. Further literature reviews should be conducted for calculating the geometry of the real shaft sectional area. Also, the density of both center guide wire and outer coils should be considered.

5.2.3 Reasonability of Dynamic Beam Theory

To use the beam theory, the shaft vibration is simplified from 3D to 2D with some assumptions. There assumptions should be reconsidered and the reasonability of dynamic beam theory should be checked.

6 Conclusion

This project focuses on three main aspects, namely the artery fabrication, centrifugal cutting force measurement, and the orbiting frequency.

The experimental table setup was first improved. The measurement data of the dynamometer in the original setup indicated significant noise which made it impossible to isolate the force caused by the grinding bit motion. This issue was resolved by grounding the dynamometer base electronically using a conducting cable. Another improvement done to the original setup was a new design of the artery fixture using T-slotted aluminum frames. This design allowed free height adjustment of the arterial path phantom to compensate for different sizes of the soft tissue phantom mounted on the fixed dynamometer fixture.

For the artery fabrication, arterial wall made of PVC was successfully fabricated. To model the actual condition during micro-grinding process inside human artery, PDMS was tested as a potential arterial wall phantom material. However, it was hard to peel a thin layer of PDMS off the aluminum rod without rolling on itself. A proposed solution was to coat the aluminum shaft with PVC before putting it into PDMS so that a thin layer of PVC allows easier aluminum shaft removal and thereby forming the artery.

Data collection of the dynamometer was improved by introducing a LabVIEW data acquisition system at a sampling rate of 5,000 Hz. This LabVIEW system allows a convenient way of comparing and verifying the data acquired throughout the experiment. Moreover, the radial force and tangential force can be decoupled by capturing the instance when the grinding wheel is at the top or bottom of the circular artery phantom for radial load and when the grinding wheel is at the left or right most end of the artery phantom for tangential load. Using MATLAB to conduct an analysis on the video captured using a high speed camera, the motion of the grinding wheel and the driving guidewire were tracked and observed. The deformation of the arterial phantom wall was also analyzed. The Fast Fourier Transform was then conducted for frequency analysis.

The driving shaft vibration was also investigated by the team. Both static and dynamic analyses were conducted. For the static analysis, the beam theory was applied with the assumption that the beam deformation was uniform in steady state. A simplified equation was obtained in the end. The static analysis model equations are in general easy to solve for estimation of the tip deflection for the first half wavelength of the driving shaft but does not reflect the actual wave and vibration situation. For the dynamic analysis, the dynamic term of the beam was considered. All assumptions in the static analysis case for the model remained the same except for the steady state assumption. An equation was obtained in the end but the 4^{th} order partial differential equation involved does not have an easy solution and is beyond the scope of this project. An alternative method of predicting the shaft vibration model is to analyze the geometry of shaft vibration from video captured during experiments and substitute the vibration geometry in the dynamic beam theory.

The rigidity of the driving shaft plays an important role in the theoretical model of the driving shaft vibration. Therefore, a “Four-Point Bending Test” was conducted to measure the rigidity. A high resolution camera and MATLAB Image Tool were used to collect and analyze the data. The rigidity of the shaft was determined to be about 4045 N-mm^2.

Despite the great result, future work for artery fabrication with PDMS, shaft vibration model, accuracy improvement of the shaft vibration model solution, property of the driving shaft and the reliability of simplified dynamic beam theory can still be conducted to improve the model.

7 References

[1] Adams, G. L., Khanna, P. K., Staniloae, C. S., Abraham, J. P., Sparrow, E.M, (2010), "*Optimal Techniques with the Diamondback 360 °System Achieve Effective Results for the Treatment of Peripheral Arterial Disease*", DOI 10.1007/s12265-010-9255-x.

[2] Morii, I., Miyazaki, S., (2000), "*Current Overview of Rotational Atherectomy. Does Rotablator Make Sense*?", Emodinamica, 22: 2-9.

[3] Nelson, G., Majewicz, A., Abraham, J., "Numerical Simulation of Thermal Injury to the Artery Wall during Orbital Atherectomy", presented at 2008 International ANSYS Conference, 2008.

[4] Tomey, M. I., Kini, A. S., Sharma, S. K., "Current Status of Rotational Atherectomy", *JACC: Cardiovascular Interventions,* vol. 7, pp. 345-353, April 2014.

[5] Reisman, M., Shuman, B. J, Harms, V., "Analysis of Heat Generation during Rotational Atherectomy Using Different Operational Techniques", *Catheterization and Cardiovascular Diagnosis,* vol. 44, pp. 453-455, 1998.

[6] "Chapter 5: Transverse Waves in Rods and Beams", Retrieved from: http://personal.egr.uri.edu/sadd/mce565/Ch5.pdf

[7] Electromagnetics Lecture notes 1&2, Retrieved from: https://ctools.umich.edu/portal

Appendix A. Project Timeline and Duty Assignment

Task Name	Duration	Start	Finish	People in Charge
Literature Review	**6 days**	**Sun 9/28/14**	**Fri 10/3/14**	**All**
Artery Fabrication	**40 days**	**Mon 9/29/14**	**Fri 11/21/14**	
Artery Properties Investigation	5 days	Mon 9/29/14	Fri 10/3/14	Di Fu, Huijiao Guan, Sing Kiet Kong
Artery Fabrication Model Building and Testing	10 days	Mon 10/6/14	Fri 10/17/14	Di Fu, Huijiao Guan, Sing Kiet Kong
Artery Fabrication	5 days	Mon 10/20/14	Fri 10/24/14	Di Fu, Huijiao Guan, Sing Kiet Kong
Artery Property Measurement and Improvement	5 days	Mon 10/27/14	Fri 10/31/14	Di Fu, Huijiao Guan, Sing Kiet Kong
Arterial Wall Mimicking using PDMS	10 days	Mon 11/10/14	Fri 11/21/14	Di Fu, Huijiao Guan, Sing Kiet Kong
Centrifugal Cutting Force Measurement	**40 days**	**Mon 9/29/14**	**Fri 11/21/14**	
Dynamometer dimension measurement	5 days	Mon 9/29/14	Fri 10/3/14	Fangzhou Xia, Xingjian Lai
Dynamometer Fixture Design and Part Ordering	5 days	Mon 10/6/14	Fri 10/10/14	Fangzhou Xia, Xingjian Lai
Dynamometer Fixture Manufacturing and Assembly	8 days	Wed 10/15/14	Fri 10/24/14	Fangzhou Xia, Xingjian Lai
Dynamometer Variable Control Testing	10 days	Mon 10/27/14	Fri 11/7/14	Fangzhou Xia, Xingjian Lai
Dynamometer Testing Data Processing	5 days	Mon 11/10/14	Fri 11/14/14	Fangzhou Xia, Xingjian Lai
Orbiting Frequency	**30 days**	**Mon 10/6/14**	**Fri 11/14/14**	
Orbiting Frequency Variable Control Testing	10 days	Mon 10/6/14	Fri 10/17/14	Fangzhou Xia, Xingjian Lai

Orbiting Frequency Testing Data Processing	10 days	Mon 10/20/14	Fri 10/31/14	Fangzhou Xia, Xingjian Lai
Verifying Orbiting Frequency Testing Data	10 days	Mon 11/10/14	Fri 11/21/14	Fangzhou Xia, Xingjian Lai
Theoretical Explanation for Grinding Wheel Motions	10 days	Mon 11/3/14	Fri 11/14/14	Fangzhou Xia, Xingjian Lai
Mathematical model for the high frequency vibration	**15 days**	**Fri 11/07/14**	**Fri 11/21/2014**	
Literature Review	8 days	Fri 11/07/14	Fri 11/14/2014	All
Design a Test to Meaure Shaft's Stiffness	10 days	Fri 11/07/2014	Tue 11/18/2014	All

Table 4: Gantt Chart of the Project